



# Diffusion processes during cementite precipitation and their impact on electrical and thermal conductivity of a heat-treatable steel

S. Klein<sup>1,\*</sup> , L. Mujica Roncery<sup>1</sup>, M. Walter<sup>1</sup>, S. Weber<sup>2</sup>, and W. Theisen<sup>1</sup>

<sup>1</sup>Lehrstuhl Werkstofftechnik, Ruhr-Universität Bochum, Universitätsstr. 150, 44870 Bochum, Germany

<sup>2</sup>Lehrstuhl für Neue Fertigungstechnologien und Werkstoffe, Bergische Universität Wuppertal, Bahnhofstrasse. 15, 42651 Solingen, Germany

Received: 6 June 2016

Accepted: 24 August 2016

Published online:

7 September 2016

© The Author(s) 2016. This article is published with open access at Springerlink.com

## ABSTRACT

The thermal conductivity of heat-treatable steels is highly dependent on their thermo-mechanical history and the alloying degree. Besides phase transformations like the martensitic  $\gamma \rightarrow \alpha'$  or the degree of deformation, the precipitation of carbides exerts a strong influence on the thermal conductivity of these steels. In the current work, thermal and electrical conductivity of a 0.45 mass% C steel is investigated during an isothermal heat treatment at 700 °C and correlated with the precipitation kinetics of cementite. To include processes in the short-term as well as in the long-term range, annealing times from 1 s to 200 h are applied. This investigation includes microstructural characterization, diffusion simulations, and electrical and thermal conductivity measurements. The precipitation of carbides is connected with various microstructural processes which separately influence the thermophysical properties of the steel from the solution state to the short-term and long-term annealing states. In the early stages of cementite growth, an interstitial-dominated diffusion reaction takes place (carbon diffusion in the metastable condition of *local equilibrium non-partitioning*). Afterwards, substitutional-dominated diffusion controls the kinetics of the reaction. The electrical and thermal conductivity increase differently during the two stages of the carbide precipitation. The increment is associated to the binding of alloying elements into the carbides and to the reduction of the distortion of the martensitic matrix. Both factors increase the electron density and reduce the electron and phonon scattering. The correlation of the precipitation kinetics and the thermophysical properties are of general interest for the design of heat-treatable steels.

Address correspondence to E-mail: klein@wtech.rub.de

## Introduction

Heat-treatable steels are frequently used in technical applications requiring defined thermal conductivities ( $\lambda_{th}$ ). Examples are tools for die casting of light metals or polymer processing. In the first case, a high thermal conductivity is beneficial to draw heat from the workpiece as fast as possible and thus to enhance productivity [1]. In the second case, lower thermal conductivities are required to prevent heat loss and freezing of the liquefied polymer mass within the production cycle [2]. In addition, the emerging trend of car manufacturing industries to produce body parts by hot sheet metal forming leads to the development of special “high thermal conductivity steels” [3, 4]. These special grades not only have to provide high  $\lambda_{th}$ -values but also high strength, toughness, and abrasive wear resistance as well as a good hardenability. The challenge in the design of new alloys is to fulfill all of these requirements in parallel. In recent years, the authors of this work and several other groups have worked intensively on the basics of thermal conductivities of heat-treatable steels to provide a fundamental understanding of the relationships between alloy composition, heat-treatment, microstructure, and thermo-physical properties [4–7].

Looking at steels from a more general point of view, maximum thermal conductivity of about  $82 \text{ W m}^{-1} \text{ K}^{-1}$  is provided by pure iron [8]. Like in every pure metal, heat conduction is primarily provided by free electrons and to a minor extent by phonons [9]. Additional effects like heat transport by magnons are often not considered for metals and will be neglected in the context of this work. Thus, the total thermal conductivity  $\lambda_{th,tot}$  is given by the sum of  $\lambda_{th,el}$  and  $\lambda_{th,ph}$  [10]. Intentional alloying with several elements and the presence of impurities are aspects that need to be considered for all technical steel grades. The presence of alloying and impurity elements reduces the thermal conductivity of iron and also influences the relative contributions of electron and phonon transport [9, 11]. Experimentally, this could be shown by Wilzer et al. using the example of C45 and X42Cr13 steel, in which the addition of 12 mass% chromium (Cr) results in a decrease of  $\lambda_{th}$  by about 45 % and shifts the phonon contribution from 27 to 55 % [12]. The relative influence of substitutional alloying elements on thermal conductivity was published by Terada et al. [11]. They investigated

binary Fe–X system with additions of 2 at.% of a broad range of elements and could show in this way that the relative reduction of thermal conductivity is highly dependent on the specific alloying element due to its position in the periodic system and electron configuration, respectively [11]. For alloy developments targeted on a maximum thermal conductivity, this implies to paying special attention to such elements with high relative influences. Based on the results of Terada et al., special attention has to be paid to chrome (Cr), manganese (Mn), and silicon (Si) while the impacts of nickel (Ni) and cobalt (Co) are less pronounced [11]. In addition, the influence of interstitially dissolved carbon (in special cases also nitrogen) has to be considered as almost all heat-treatable steels are carbon-alloyed.

The previous explanations considered the presence of alloying and impurity elements in a homogeneous solid solution. In heat-treatable steels, this case can be approximated by fast quenching from a homogeneous austenitic single-phase condition. The approximation indicates that non-metallic inclusions are not dissolved during austenitization and carbon segregation effects during quenching cannot be fully ruled out. This also holds for macroscopic and microscopic segregations of substitutionally dissolved elements. The presence of retained austenite in the as-quenched condition can be minimized by low levels of alloying, in particular with carbon, and an additional cryogenic treatment [13]. Assuming a homogeneous one-phase  $\alpha$ -martensitic condition after quenching, the relative influence of alloying elements can be directly implemented. However, heat-treatable steels are usually put into service in a tempered condition or at least after a relaxation heat treatment. The one-phase  $\alpha$ -martensitic condition is thus transformed at least to a two-phase state including the tempered martensitic matrix and carbides. The literature found in this context is scarce, in particular concerning the influence of heat treatment, resulting microstructures and temperature on resulting thermal conductivities of steels. Wilzer et al. published comparative experimental results on the impact of heat treatment on room temperature thermal conductivity of three differently alloyed steels exhibiting comparable carbon levels [14]. In their work, the impact of carbide precipitation from a supersaturated fully  $\alpha$ -martensitic state is emphasized. Furthermore, the importance of matrix

composition in tempered states is discussed. The authors show that the chemical composition of the tempered  $\alpha$ -martensitic matrix dominates the thermo-physical properties, while the direct influence of carbide precipitates is of minor importance. In general, thermal conductivity increases continuously with tempering temperature. In another work, the same authors investigated the influence of temperature on the thermal conductivity of steels [15]. Here, the pronounced effects of phonon and electron scattering with increasing temperatures are emphasized. In addition, the changes of electronic states of high-Cr steels are discussed, serving as an explanation for increasing thermal conductivities with temperature.

Earlier researchers investigated the precipitation behavior of cementite, most notably Abe and Suzuki [16], Abe et al. [17] and Hanawa and Mimura [18], without accounting for the impact on thermal conductivity. They investigated the effect of carbon clustering and precipitation on the electrical resistivity and thermoelectric power of a 0.046 mass%-C steel after aging at temperatures spanning from 35 to 300 °C [16]. When aged at 300 °C, they observed a complete precipitation of cementite after 100 s. Moreover, they could derive information about the coherency of the precipitates from the slope of the thermoelectric power versus electrical conductivity plot. In another work, they could separate the aging process into the distinct stages of clustering and precipitation of carbon by correlating electrical conductivity with the thermoelectric power after strain-aging. In an additional step, they compared the hardening effect with the earlier results and concluded a lack of clustering of carbon atoms when aged at temperatures above 100 °C [17].

In fact, the shortest aging time they achieved was 2 s, which allows the assumption that the clustering stage was already completed at this time, which could only be validated by diffusion simulation. In addition, the content of Cr in the steel is omitted and no higher temperatures were investigated, leaving the question of substitute-driven precipitation open. In a work by Song et al., the authors correlated diffusion simulations with the chemical composition of cementite by means of EDS and atom-probe measurements [19]. They investigated the precipitation kinetics in 100Cr6 bearing steel and found the precipitation mode to be LEMP at 800 °C.

Most experimental works on thermal conductivities of steels found in literature have one aspect in common: they either concentrate on a virtually homogeneous supersaturated state or consider quenched and tempered conditions after a technical heat treatment. From a technological point of view, this approach is useful, but it fails to provide information on either the first stages of tempering or on the equilibrium state that is reached after long-term tempering. The following scientific questions were thus deduced:

- (1) Which mechanisms take place during cementite precipitation and growth and how do they relate to the resulting thermal conductivity?
- (2) How fast does the carbide precipitation from a homogeneous supersaturated condition of a heat-treatable steel take place?
- (3) How long does it take to reach the equilibrium contents in matrix and carbides?
- (4) What is the quantitative impact of carbon depletion from an  $\alpha$ -martensitic condition on thermal conductivity?
- (5) What is the quantitative impact of substitutional element depletion on thermal conductivity during long-term tempering?

To find answers to these questions, the non-alloyed heat-treatable steel DIN EN 1.1141 (C45E) was investigated in this work experimentally and by the simulation of carbide precipitation kinetics. The high velocity of these processes during tempering enforced several special approaches explained in detail in the following paragraph.

## Methods

### Material

The investigated steel C45E (DIN EN 1.1141, AISI, SAE, ASTM 1045) was supplied in normalized and rotary swaged condition by Deutsche Edelstahlwerke. The rods had a diameter of about 50 mm. Specimens were extracted by wire erosion cutting. The specimens for laser-flash analysis were cut facing in axial direction and had dimensions of 10 mm × 10 mm × 1.5 mm. The specimens for electrical resistivity measurements were 20 mm long with a diameter of 5 mm and were cut axially parallel.

**Table 1** Chemical composition of the investigated steel determined by optical spark emission spectrometry

Units	C	N	B	Mn	Cr	Cu	Ni	Si	P	S	Mo	Co	Sn
Mass%	0.463	<0.0012	<0.0001	0.661	0.178	0.167	0.114	0.289	0.016	0.025	0.021	0.006	0.008
at.%	2.112	<0.0047	<0.0005	0.659	0.188	0.144	0.106	0.494	0.028	0.049	0.012	0.006	0.004

Iron is the dependent substitutional element

## Chemical composition

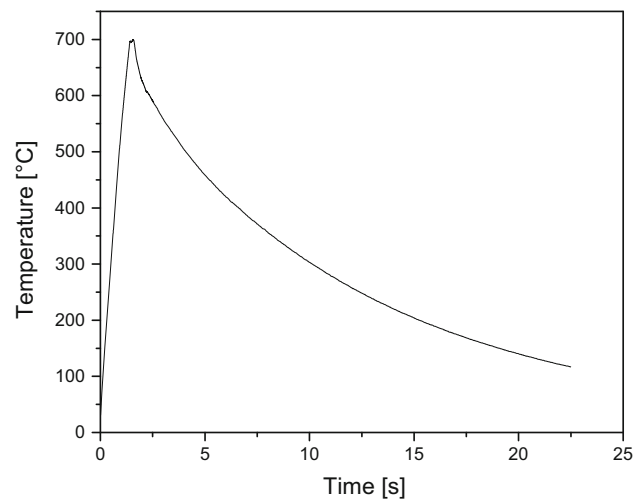
In this study, the tool-steel C45E is investigated in different heat-treated conditions. The mean chemical composition of the material used in this study was determined by optical spark emission spectrometry and is listed in Table 1. Besides the carbon content of 0.46 mass%, which is responsible for the martensitic hardenability, C45E steel contains certain amounts of C, Mn, Si, Cr, Ni, and Cu.

## Heat treatment

The first heat treatment step for all the material consisted of austenitization in a special high-vacuum, radiation furnace with Mo heaters at 900 °C for 20 min followed by water quenching. The furnace used allows very quick water cooling by an integrated water bath, in which the material falls in directly from the heating chamber. This was crucial for a successful martensitic hardening of C45E, since pearlite formation starts after about 2 s. After water quenching, the material was deep cryogenically treated (DCT) and stored in liquid nitrogen for 30 min. Specimens for short-term aging (for dwell times 1 and 10 s) were kept in liquid nitrogen until aging and between aging and measurement. Subsequently, aging was performed at 700 °C according to the following procedures. The specimens for the electrical resistivity measurements in not-aged condition were kept in liquid nitrogen and immediately measured at room temperature. This should prevent undesired aging at ambient temperature.

### Short-term aging of specimens

The short-term aging at 700 °C was carried out in a Dil 805 quenching dilatometer from BÄHR-Thermoanalyse GmbH. To control the temperature, a type K thermocouple was attached on the surface of each specimen by spot welding. In the dilatometer, the

**Figure 1** Temperature–time plot of the shortest aging time of 1s.

specimens were inductively heated under vacuum conditions. The mean heating rate was 493 K s<sup>-1</sup> resulting in a heating up time of only 1.4 s. After dwelling for 1, 10, 100, 720, and 7200 s, samples were quenched using compressed helium gas. The cooling rate starts with about 130 K s<sup>-1</sup> and diminishes below 650 °C. The absolute aging time is given by the total time above 650 °C. The temperature–time plot of the shortest aging process is shown in Fig. 1. To verify the heat treatment, Vickers hardness of each specimen was measured before and after aging.

### Long-term aging of specimens

For long-term aging, inert gas convection furnaces were used. The specimen were wrapped in high alloyed steel foil to reduce oxidation and isothermally heat treated at 700 °C for 720, 7200, 72000, and 720000 s followed by oil quenching.

## Microstructural analysis

The microstructural analyses were performed by means of scanning electron microscopy (SEM) using

a LEO 1530VP field emission SEM from Zeiss Microscopy GmbH. For this purpose, samples were polished to a surface grade of 1  $\mu\text{m}$  using diamond polishing suspension. Etching or other possibilities of creating topographic surface contrasts were avoided carefully. SEM analysis was done using secondary electron (SE) contrast, an acceleration voltage of 10 kV and a working distance of 15 mm.

Image analysis of the SEM images was performed with the software ImageJ [20]. For each state, three SEM images of 10k to 25k magnification were analyzed. Image analysis was performed using the following steps: scaling of the image, adjustment of brightness and contrast for maximum particle-matrix disparity, binarization of the image, adjusted post-processing of the binary image with regard to the comparability to the original SEM image. After this processing of the images, results were generated using the *analyze particles* command. For the evaluation of the particle size, particles on the edge of the image or with a particle size below 10 nm were excluded. Results are referred to the total image area. Image and particle parameters used in this study are the total particle volume fraction, the maximum and minimum Feret diameters and the average particle distance. Results are displayed as arithmetic average values including standard deviations.

### X-ray diffraction using line-profile analysis

Microstructural analysis of the lattice parameter of C45E steel in as-hardened and in quenched and tempered condition was performed by means of X-ray diffraction (XRD) using line-profile analysis (LPA; Rietveld-analysis [21]). Investigations were performed using a diffractometer type Bruker D8 Advance and the Rietveld-analysis software MAUD [22, 23]. The diffraction experiments were conducted using the following parameters: Cu  $K\alpha$  (Cu  $K\alpha_1 = 1.54060 \text{ \AA}$  and Cu  $K\alpha_2 = 1.54439 \text{ \AA}$ ) radiation, Lynx-Eye detector, detector divergence slit size of 1 mm,  $2-\Theta$  angle range of  $25^\circ$ – $100^\circ$ , measurement step size of  $0.005^\circ$ , and a measurement time of 1 s per step. Cu  $K\beta$  radiation was suppressed by the use of a Ni-filter in front of the radiation tube. The measurements were done while rotating the sample.

The microstructural analysis of the XRD-pattern was done using the software MAUD. The evaluations were done using  $\text{Al}_2\text{O}_3$  (COD-file 1000032) reference material. The phase evaluated was bcc-iron (ferritic

steel, COD-file 9008536) only. Analysis was performed as microstructural line broadening analysis of the ferritic bcc lattice, to determine the change in bcc lattice parameter due to a lattice distortion. Line broadening modeling was done according to Popa and Balzar [24], Balzar and Popa [25] considering a grain size larger 30  $\mu\text{m}$ .

### Electrical and thermal conductivity

#### Measurement of thermal conductivity

The dynamic method described by [10, 26] was used to measure the thermal conductivity of the long-term aged specimens. To do so, the specific isobaric heat capacity  $c_p$ , density  $\rho$  and thermal diffusivity  $\alpha$  were measured independently. Afterwards, the thermal conductivity  $\lambda$  was calculated using Eq. 1. Its unit is  $\text{W m}^{-1} \text{K}^{-1}$ .

$$\lambda = c_p \cdot \rho \cdot \alpha. \quad (1)$$

To obtain the specific isobaric heat capacity  $c_p$ , a modulated differential scanning calorimeter mDSC 2920 CE from TA Instruments was utilized with Pt/Rh pans and lids. Measurements took place in a dynamic He atmosphere with a flow rate of 120  $\text{L h}^{-1}$ . For ambient temperature measurement, a linear, sinusoidally modulated temperature ramp was imposed, starting at  $-30^\circ\text{C}$  and heating with  $10 \text{ K min}^{-1}$  to  $50^\circ\text{C}$ . The modulation had an amplitude of 1 K with a period of 1 min.

The thermal diffusivity was measured with the laser flash method. The device used was a LFA 1000 from Linseis Messgeräte GmbH. Measurements were made in vacuum. The dimensions of the specimens were 10 mm  $\times$  10 mm  $\times$  1.5 mm. Before measurement, the specimens were ground with 1000 mesh abrasive paper.

Density was measured according to the Archimedes buoyancy principle utilizing a high precision balance with an accuracy of 0.1 mg. All specimens were measured five times in ethanol.

#### Measurement of electrical conductivity

Electrical conductivity of the short-term aged specimens was measured utilizing the four-wire method (also known as *four terminal sensing* or *four point probe method*). The current was set to 100 mA. For each specimen, five measurements were performed at

ambient temperature. In the plots, the mean values and standard deviations of those five measurements are shown. All specimens were ground with 1000 mesh abrasive paper before the measurement to remove oxide layers.

### Conversion of electrical and thermal conductivity

The electrical conductivity and the thermal conductivity are converted by Wiedemann–Franz–Lorenz law, given in Eq. 2. This relation is used to plot Fig. 4. The unit of the electrical conductivity is  $\mu\Omega^{-1} \text{ m}^{-1}$ . It should be noted that the calculated thermal conductivity considers only the electronic heat transfer; thus, it is always lower than the measured thermal conductivity [10].

$$\frac{\lambda_e}{\sigma} = L_0 \cdot T \sigma = \frac{\lambda_e}{L_0 \cdot T}. \quad (2)$$

The Lorenz constant  $L_0$  is calculated using the Boltzmann constant  $k_B$  and the elementary charge  $e$  according to Eq. 3 [10].

$$L_0 = \frac{\pi^2}{3} \left( \frac{k_B}{e} \right)^2 L_0 \approx 2.44 \times 10^{-8} \text{ V}^2 \text{ K}^{-2}. \quad (3)$$

### Thermodynamic calculations and diffusion simulations

The thermodynamic calculations and diffusion simulations were performed applying the CALPHAD method. Thermo-Calc S, Dictra software 27 and the databases TCFE7 and MOBFe2 were employed, all from Thermo-Calc Software AB. For the calculations, only the elements Fe, C, Cr, Mn, Si, and Ni were included according to the chemical composition given in Table 1. All the calculations were performed isothermally at 700 °C, the heat-treatment temperature. The approach for this calculation is similar to that reported previously in the literature [27–29].

In order to set up the composition of the cementite nucleus, thermodynamic calculations were performed in Thermo-Calc. The martensitic matrix (BCC\_A2) had the alloy composition and was an active phase, whereas cementite was a dormant phase. Other phases were suspended. Under these conditions, the composition of the cementite was calculated and the driving force of the precipitation was obtained (Table 2). The estimated driving force for the precipitation is 7583.7 J mol<sup>-1</sup>.

**Table 2** Composition of the matrix and the cementite nucleus determined with Thermo-Calc and used as input for the kinetic simulations

Phases	C	Cr	Mn	Ni	Si	Fe
Matrix	2.11	0.19	0.66	0.11	0.56	Bal.
Cementite	25.00	3.25	4.56	0.02	$7.5 \times 10^{-11}$	Bal.

Values in at.%

The diffusion processes during cementite precipitation were calculated using the Dictra software with a single cell system, composed of a martensitic matrix (BCC\_A2 phase supersaturated in C, the closest approach to the real matrix) and a cementite M<sub>3</sub>C nucleus. The matrix composition was equal to that of the substrate and the nucleus composition was given by the thermodynamic calculations. The geometry was defined as circular; the matrix had a radius of 30 μm, distance adjusted according to the initial microstructure. The nucleus had a radius of 2 nm, larger than the critical radius of 0.7 nm to ensure stability of the calculation. The system was kept isothermally throughout the complete simulation time. The total simulation time was 720,000 s (200 h).

## Results

### Carbide precipitation and growth during heat treatment

The resulting microstructures observed by means of SEM of C45E steel after heat treatment are shown in Fig. 2. In the quenched + DCT state, C45E steel shows an entirely martensitic microstructure without the presence of carbides. This state does not change significantly during short time tempering for 1–10 s. After 100 s of tempering time, carbides are well detectable in the microstructure of C45E steel. These carbides are mainly distributed along the grain boundaries and grow with increasing tempering time, as seen in Fig. 2. A connected process is the simultaneous increase of the grain size with the carbide size. As a result, the specimen tempered for the maximum tempering time of 720,000 s shows a microstructure consisting of large carbides and grains.

Table 3 and Fig. 3 show the results of the parameters determined by quantitative image analysis of

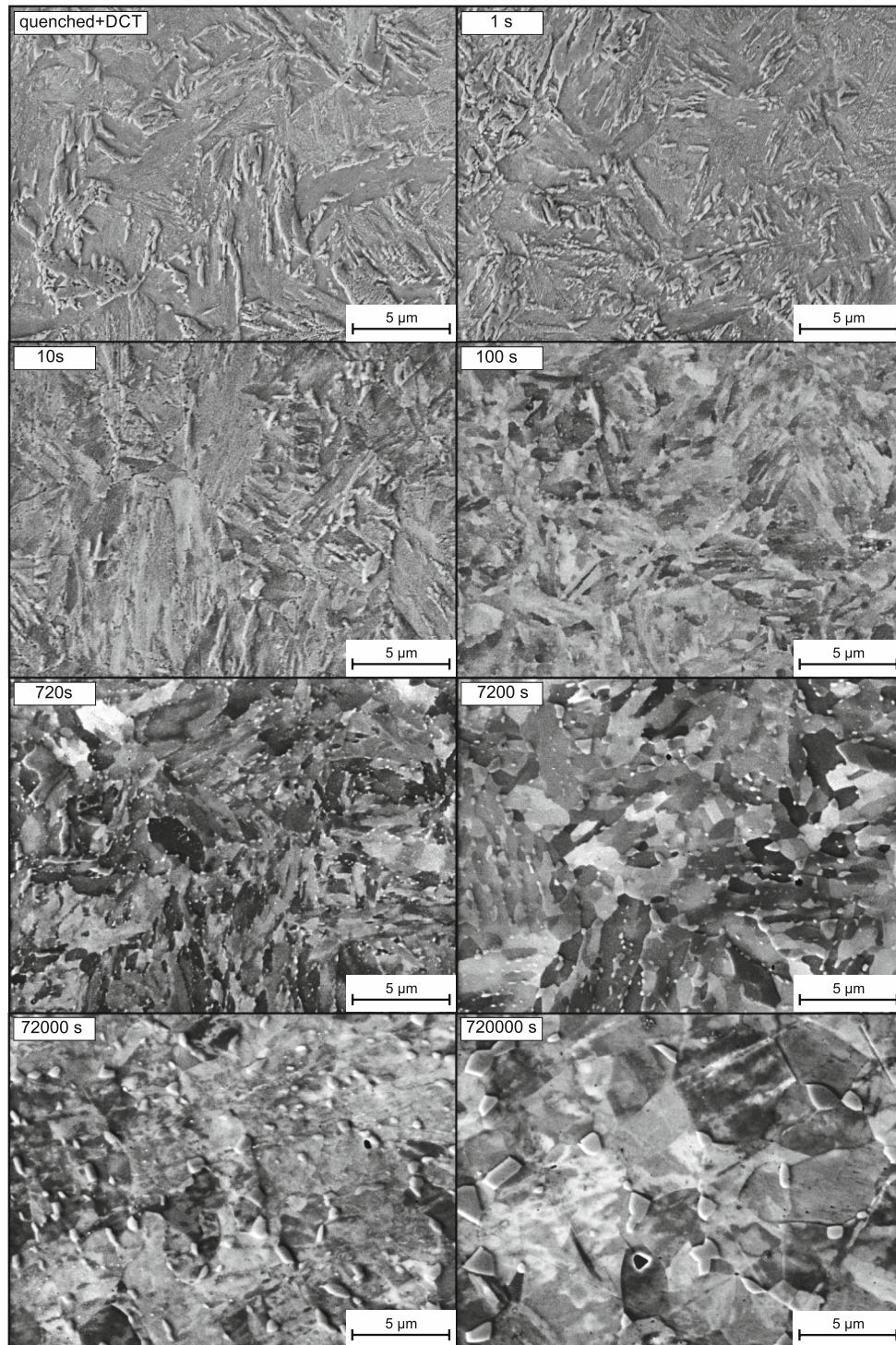


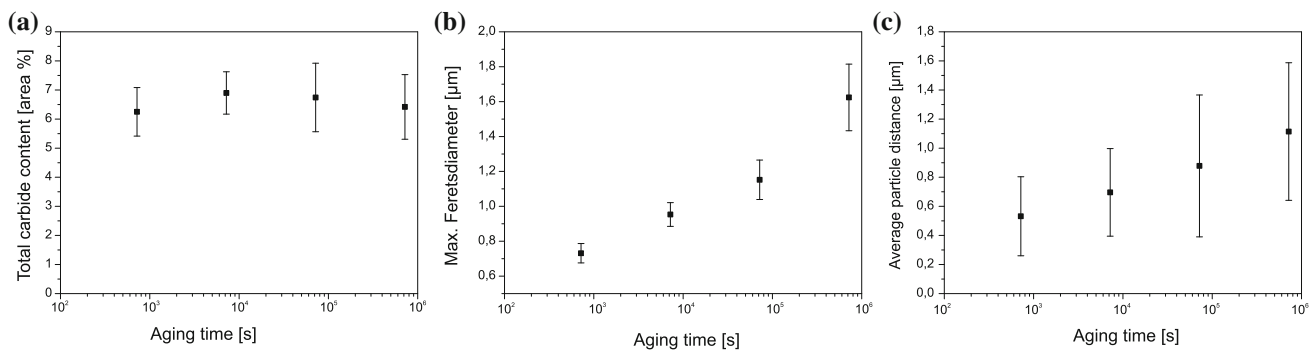
**Figure 2** Resulting microstructure of C45E in the as-quenched + DCT (deep cryogenically treated) condition and after isothermally aging for 1–720,000 s at 700 °C.

the quenched and tempered C45E steel microstructure. Results are presented for tempering times longer than 100 s and in logarithmic ( $\log_{10}$ ) scale. Results show, on the one hand, a continuous increase

of carbide size and distance with increasing tempering time and on the other hand, a constant, unchanged carbide volume content from 100 to 720,000 s of tempering time.

**Table 3** Quantitative image analysis: results of the determined parameters of C45E steel in quenched and tempered state

Tempering time (s)	Carbide content (area %)	Max. Ferets-diameter ( $\mu\text{m}$ )	Distance between particles ( $\mu\text{m}$ )
0–100	Not detectable	Not detectable	Not detectable
720	$6.25 \pm 0.83$	$0.73 \pm 0.05$	$0.53 \pm 0.27$
7200	$6.89 \pm 0.72$	$0.95 \pm 0.06$	$0.69 \pm 0.30$
72,000	$6.74 \pm 1.17$	$1.15 \pm 0.11$	$0.88 \pm 0.48$
720,000	$6.42 \pm 1.11$	$1.62 \pm 0.19$	$1.11 \pm 0.47$

**Figure 3** Quantitative image analysis of C45E steel in quenched and tempered state. **a** Total carbide content. **b** Maximum Feret diameter of the carbides. **c** Average distance between particles.

### Thermal conductivity after aging

The resulting thermal and electrical conductivity of the steel C45E after annealing is shown in Table 4 and Fig. 4. In the as-quenched state, the steel C45E exhibits a calculated thermal conductivity of  $25.6 \text{ W m}^{-1} \text{ K}^{-1}$ . When aged, its thermal conductivity increases rapidly. Already after 1 s of annealing at  $700 \text{ }^\circ\text{C}$ , the thermal conductivity increases to  $35.8 \text{ W m}^{-1} \text{ K}^{-1}$ . Afterwards, the thermal conductivity rises slowly to  $38.3 \text{ W m}^{-1} \text{ K}^{-1}$  after an aging time of 7200 s. While the thermal conductivity of these short-term annealed specimens could only be calculated from the measured electrical conductivity (due to specimen size restrictions), the measured thermal conductivity of the long-term annealed specimens shows a similar behavior in the range of 720–7200 s, confirming the validity of the calculated thermal conductivity with a difference of approximately 5 %. As already mentioned, calculated  $\lambda_{\text{th}}$  values are lower than measured ones due to the neglected influence of phononical heat transport. Effectively, calculated values represent  $\lambda_{\text{th,el}}$ , whereas measured values are a combination of  $\lambda_{\text{th,ph}}$  and  $\lambda_{\text{th,el}}$  ( $=\lambda_{\text{th,tot}}$ ). Additionally,

the long-term annealed specimens show a gradual increase of the thermal conductivity from  $40.6$  to  $41.2 \text{ W m}^{-1} \text{ K}^{-1}$  between 7200 and 72,000 s. Until an aging time of 720,000 s it stays almost constant with a minor increase to  $41.5 \text{ W m}^{-1} \text{ K}^{-1}$ .

Because of the geometric requirements for the laser-flash specimens, they could not be short-term annealed as described in “Short-term aging of specimens” section. Thus, it was not possible to measure the thermal conductivity for the short dwell times of 1, 10, and 100 s. To accommodate this restriction, the electrical conductivity has been measured, which allows smaller, cylindrical specimens to be measured. As described in Conversion of electrical and thermal conductivity section, the electronic contribution to the thermal conductivity  $\lambda_e$  can be calculated from the electrical conductivity  $\sigma$ . Although  $\lambda_e$  is not equal to  $\lambda$ , it allows the discussion of influencing factors on the thermal conductivity when affecting the electronic heat transport. To get an indication on the influence on the changes to the phononical heat transport, the difference  $\lambda - \lambda_e$  and the fraction of electronic heat transport  $\frac{\lambda_e}{\lambda}$  can be taken in account (Table 4).



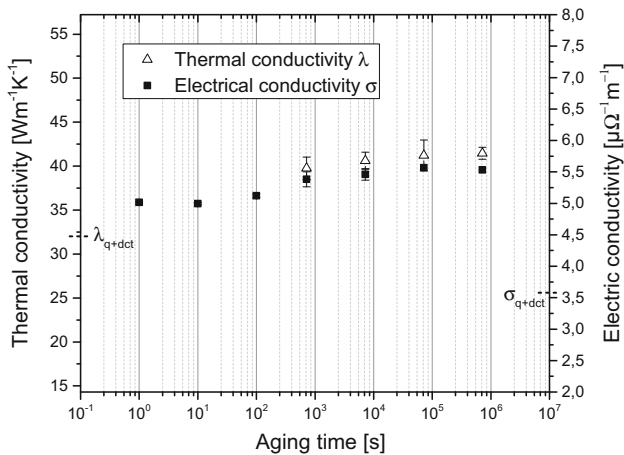
**Table 4** Measured electrical and thermal conductivity of C45E at 20 °C after annealing at 700 °C and quenching

Annealing time at 700 °C	Thermal conductivity $\lambda$ (W m <sup>-1</sup> K <sup>-1</sup> ) (measured)	Electrical conductivity $\sigma$ ( $\mu\Omega^{-1}$ m <sup>-1</sup> ) (measured)	Thermal conductivity $\lambda_e$ (W m <sup>-1</sup> K <sup>-1</sup> ) (Eq. 2)
As-quenched	32.08 ± 2.31	3.588 ± 0.025	25.65 ± 0.18
1 s	–	5.014 ± 0.021	35.84 ± 0.15
10 s	–	4.994 ± 0.020	35.70 ± 0.14
100 s	–	5.121 ± 0.031	36.61 ± 0.22
720 s (12 min)	39.75 ± 1.27	5.382 ± 0.117	38.47 ± 0.84
7200 s (2 h)	40.61 ± 0.98	5.460 ± 0.091	39.03 ± 0.65
72,000 s (20 h)	41.21 ± 1.43	5.565 ± 0.049	39.79 ± 0.35
720,000 s (200 h)	41.46 ± 1.21	5.532 ± 0.055	39.55 ± 0.39

Annealing time at 700 °C	Thermal conductivity $\lambda_p$ (W m <sup>-1</sup> K <sup>-1</sup> )( $\lambda - \lambda_e$ )	Fraction of electrical heat conduction ( $\lambda_e/\lambda$ )	Lattice parameter $a_{bcc}$ (Å) (“X-ray diffraction using line-profile analysis” section)
As-quenched	6.43 ± 2.31	0.80	2.8781
1 s	–	–	2.8693
10 s	–	–	2.8687
100 s	–	–	2.8686
720 s (12 min)	1.28 ± 1.52	0.97	2.8684
7200 s (2 h)	1.57 ± 1.18	0.96	2.8683
72,000 s (20 h)	1.43 ± 1.48	0.97	2.8679
720,000 s (200 h)	1.91 ± 1.28	0.95	2.8672

The thermal conductivity  $\lambda$  is calculated using measured values of  $c_p$ ,  $\rho$  and  $\alpha$  according to Eq. 1. The lattice constant at 20 °C is derived from XRD measurements using the line-profile analysis, as described in “X-ray diffraction using line-profile analysis” section. The lattice parameter of a reference bcc iron cell is 2.8665 Å



**Figure 4** Thermal and electrical conductivity of C45E at 20 °C after annealing at 700 °C and quenching, transformed according to Eq. 2. Points marked by *triangles* are measured thermal conductivities  $\lambda$ . Points marked by *filled squares* represent the measured electrical conductivities  $\sigma$ . The *dotted lines* on the *y-axis* mark the measured thermal and electrical conductivity  $\lambda$  directly after quenching and deep cryogenic treatment.

### Simulation of diffusion processes during heat treatment

The simulation results show two stages of cementite growth: the first one close to 0.01 s, where the cementite volume fraction reaches 3.5 vol.%, and a second stage where the volume fraction increases to 6.5 vol.% and remains constant (Fig. 5a). The same behavior is reflected in the carbide radii, which reach a maximum of 120 nm (Fig. 5b).

The fact that the volume fraction reaches the equilibrium volume fraction after a few seconds does not mean that it has reached the chemical equilibrium. In Fig. 5c, it can be seen that in the first seconds there is a rapid decrease of carbon content in the martensitic matrix, which has diffused for the formation of the cementite. On the one hand, carbon has a relatively high diffusivity as an interstitial element in the bcc matrix compared to that of the substitutional elements. On the other hand, in this system, the

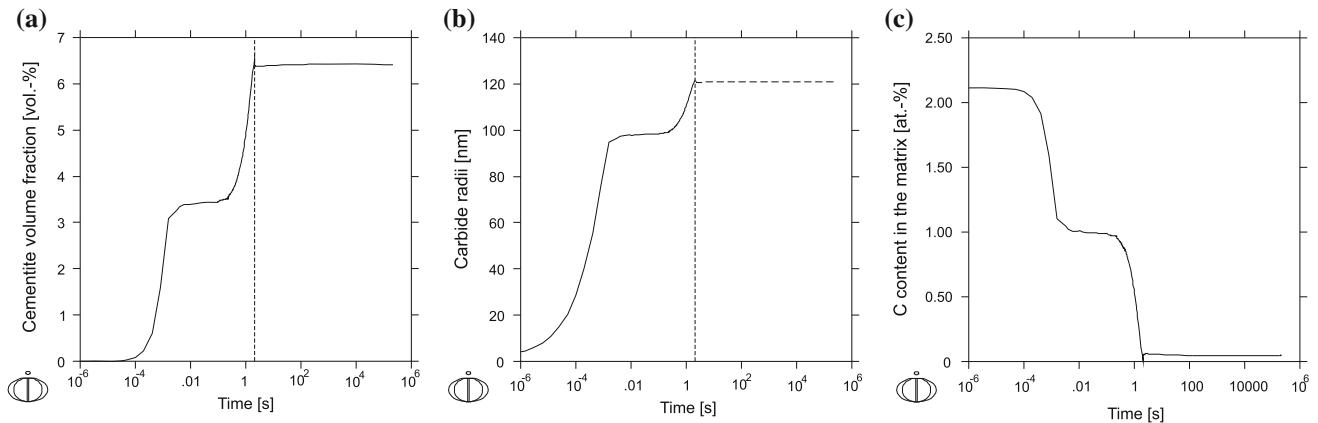


**Figure 5** Simulation results. **a** Cementite volume fraction evolution during aging. **b** Carbide radii in dependence of time. After reaching the equilibrium volume fraction (marked by the vertical line), the simulated carbide radius cannot increment further due to

C activity in the matrix ( $a_C = 10.0$ , reference state Graphite, 298 K), compared to that of the cementite with the same Cr/Fe and Mn/Fe ratios ( $a_C = 3.4 \times 10^{-4}$ , reference state Graphite, 298 K) is significantly higher. This means that carbon diffusion controls the formation of cementite in the metastable condition of local equilibrium non-partitioning (LENP) [28], where the cementite and the matrix have the same ratio of substitutional elements (Cr, Mn, Fe, Ni, Si). This can be observed in Fig. 6. After 1 s, the cementite has reached more than 100 nm size and is easily recognized thanks to the stoichiometric carbon content of 25 at.%. In contrast, Mn and Cr contents in the cementite have approximately the same content as in the matrix. Due to the low solubility in the carbide, Si accumulates in the martensitic region at the interface. The LENP mechanism is also related to the first plateau observed in Fig. 5 in the early stages of the cementite formation. After 100 s, the elements Mn and Cr diffuse towards the carbide and accumulate in the cementite at the interface, where a sharp peak is observable (Fig. 6a, b). In contrast to Cr and Mn, Si accumulates in the matrix (Fig. 6c).

After long-term aging, the diffusion of the substitutional elements Cr and Mn inside the cementite plays a major role. In Fig. 7, the partitioning of Cr and Mn in the matrix and in the cementite at different times with respect to the distance in the cell can be observed, as well as the integrand Cr and Mn contents in the matrix in dependence of time. After 720 s, Cr accumulates at the carbide interface reaching

neglecting the ongoing Ostwald-ripening, which is represented by a dotted line.

3 at.%. As the time proceeds, the Cr and Mn diffusion inside the carbide gradually increases and the martensitic matrix is therefore depleted of these elements, as seen in Fig. 7. In this case, the system drives towards the global equilibrium, where very low (almost negligible) interface velocity is visible, and the transformation is governed by the slowest diffusing species.

## Discussion

The resulting volume fraction from the diffusion calculations (Fig. 5a) aligns well with the measured carbide fraction (Fig. 3a). One point of disagreement is the measured particle size (Fig. 3b), because Ostwald ripening is not considered in the Dictra simulation (Fig. 5b). Since Ostwald ripening does not imply an increment of the volume fraction or a change of the equilibrium composition of the matrix, this is not considered as a critical point. As indicated in the previous section, the growth mechanism of cementite in the short-term annealing is considered as LENP [28], where the differences in the C-activity between the matrix and the carbide controls the kinetics. This differs from the paraequilibrium mechanism, where the growth is controlled by the fastest diffusion species when the diffusivity of the substitutional species is negligible compared to that of interstitial species. At the tempering temperature, the diffusivity of the substitutional species in the bcc matrix is lower than that of carbon (Table 5).

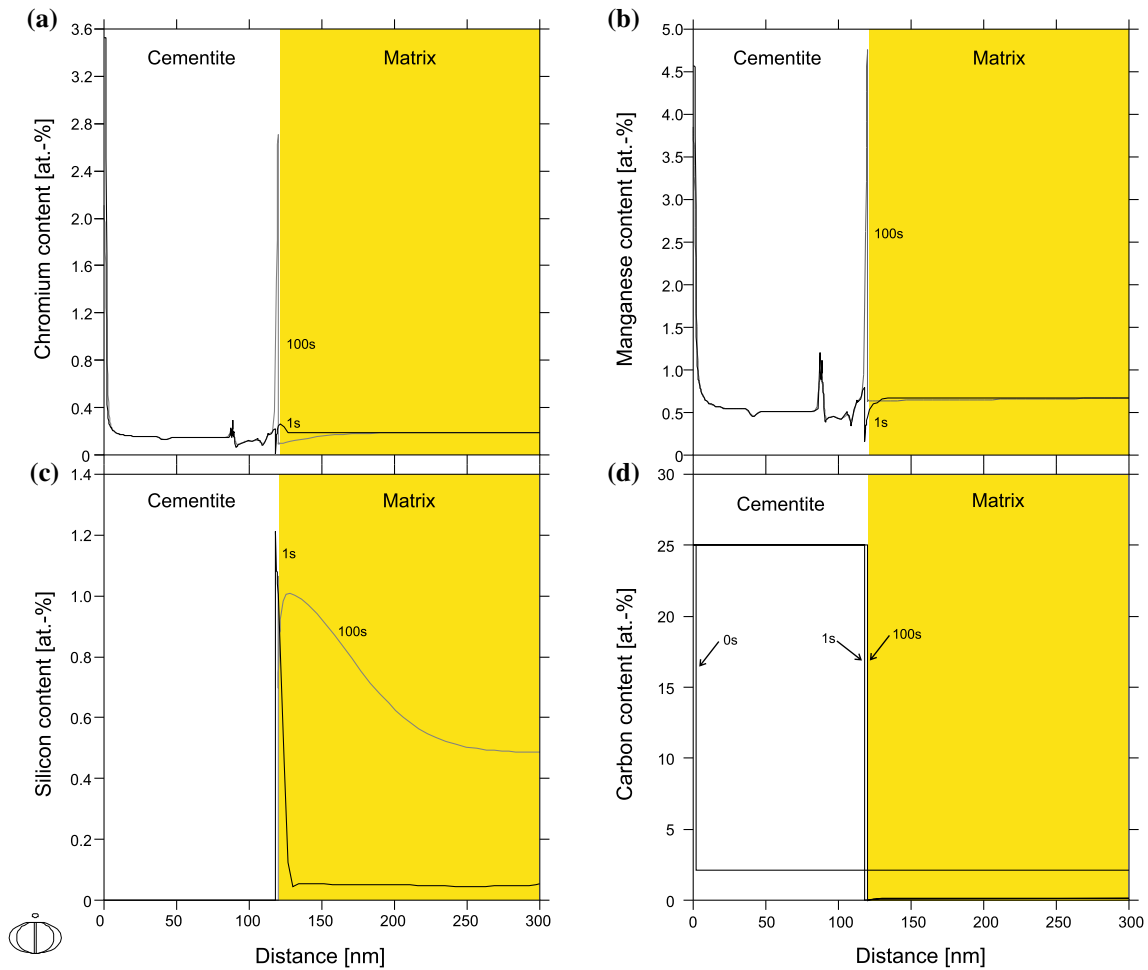


**Figure 6** Element content in the first seconds of the cementite formation during short-term aging at 1 and 100 s. The matrix region is highlighted in yellow background as an orientation, according to the position of the carbide/matrix interface at time

100 s. **a** Cr content. **b** Mn content. **c** Si content. **d** Carbon content: the time 0 s is indicated with a dotted line, and the position of the interface is indicated with arrows, from 0 to 1 s the carbide grows more than 100 nm.

According to Inden et al., the point of the transition from para-equilibrium to LEMP can be estimated by comparing the velocity of the interface between carbide and matrix  $v_i$ , with the diffusion velocity  $v_d$  [28]. The average diffusion distance  $\bar{x}$  is estimated to be four bcc unit cells, which is about  $11 \times 10^{-10}$  m in bcc steel [28]. The time  $t_d$  needed to diffuse through this distance is then given by Eq. 4. With this, the diffusion velocity can be calculated by Eq. 5. The resulting values for the elements considered are given in Table 5.

$$t_d = \frac{\bar{x}^2}{2D}, \tag{4}$$

$$v_d = \frac{\bar{x}}{t_d}, \tag{5}$$

$$v_i > v_d. \tag{6}$$

For LEMP to be the active precipitation kinetic, the interface velocity  $v_i$  must be greater than the diffusion velocity  $v_d$  (Eq. 6). At the beginning of the simulation, the interface velocity is  $v_d = 4 \times 10^{-4} \text{ m s}^{-1}$ . As shown in Table 5, all substitutional elements meet this requirement. A constrained diffusion should therefore be discarded.

One point to analyze is the increase in the thermal and electrical conductivity from as-quenched to annealed state (see Fig. 4). This occurs because of the fast diffusion of carbon and the depletion of this element in the very early stages of annealing, as shown in Fig. 5c, accompanied with the fast carbide formation (Fig. 6d) during short-term aging. Other diffusing species such as Si may play a secondary role in this stage, since it keeps a global

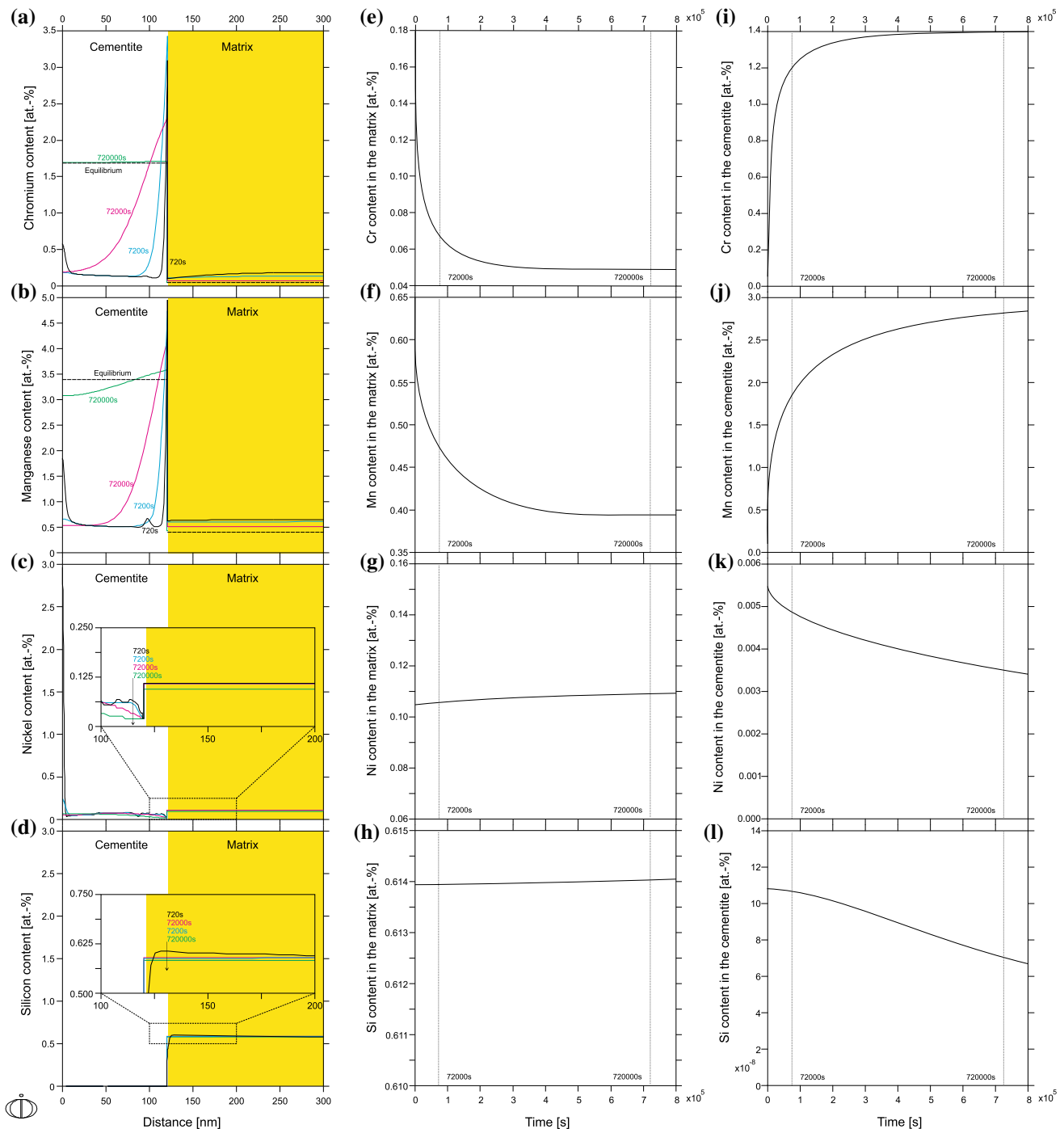


**Figure 7** Diffusion of substitutional elements Cr, Mn, Ni, and Si during long-term aging (see “Heat treatment” section). Content of Cr, Mn, Ni, and Si (a–d) in the simulation cell for selected times.

constant value in the matrix due to its almost incipient solubility in the carbide. Nevertheless, Si influences the thermal conductivity of the matrix and the activity of the other components and thus affects the growth kinetics implicitly. As previously

discussed, Cr, Si, Ni, and Mn diffuse very slowly and they keep the same composition in the matrix (Fig. 6a, b) and should not be responsible for the increase of conductivity in the first seconds of aging.

Evolution of the Cr, Mn, Ni, and Si contents in the matrix (e–h) and in the cementite (i–l) during aging.

**Table 5** Diffusion coefficients  $D$  at 700 °C of the elements which were considered in the simulation, calculated average diffusion time  $t_d$  and average diffusion velocity  $v_d$

Values	Units	C	Ni	Mn	Si	Cr
$D$	$\text{m}^2 \text{s}^{-1}$	$5.47 \times 10^{-11}$	$8.50 \times 10^{-18}$	$2.24 \times 10^{-17}$	$1.34 \times 10^{-17}$	$5.38 \times 10^{-18}$
$t_d$	s	$1.11 \times 10^{-8}$	$7.12 \times 10^{-2}$	$2.70 \times 10^{-2}$	$4.51 \times 10^{-2}$	$1.12 \times 10^{-1}$
$v_d$	$\text{m s}^{-1}$	$9.95 \times 10^{-2}$	$1.55 \times 10^{-8}$	$4.07 \times 10^{-8}$	$2.44 \times 10^{-8}$	$9.78 \times 10^{-9}$

$t_d$  and  $v_d$  are calculated according to Eqs. 4 and 5

By combining the results from diffusion simulation and conductivity measurements, the change of the thermal and electrical conductivity over the annealing time can be divided in two intervals.

In the first interval, from the beginning of the annealing process to about 2 s, the thermal and electrical conductivity of the steel is mainly influenced by the increment of carbide volume fraction and the depletion of the martensitic matrix from carbon. In this interval, several microstructural processes take place simultaneously. Obviously, the increasing volume fraction of cementite reduces the carbon content of the matrix, as shown in Fig. 5c. Since carbon reduces the density of free electrons [30, 31], binding carbon in the cementite increases both the electrical conductivity as well as the electronic part of the thermal conductivity of the matrix. The size of the formed carbides is rather small (less than 1  $\mu\text{m}$ ), so their interfacial character as a resistance is much stronger than their contribution to the conductivity. So, regarding their influence on thermal and electrical conductivity, they behave like vacancies [32]. As a result, the conductivity of the carbide itself and, up to a specific value, its size does not influence the conductivity of the steel. The thermal and electrical resistance of the cementite precipitates is overcompensated by the reduction of matrix resistance due to carbon depletion.

Another process taking place in the first interval is the relaxation of the martensite, where the tetragonal distortion of the matrix is reduced. This process is closely connected to the removal of carbon from the supersaturated matrix. One effect of the relaxation is the reduction of phonon scattering centers which originate in the strain field of a distortion [33]. This results in a higher phonon thermal conductivity  $\lambda_p$  [34]. Since the change in conductivity during the first interval could only be measured by means of electrical conductivity, this effect is not detectable in this range. However, the precipitation of the cementite adds a lot of new resistances due to the addition of interfaces, which reduces  $\lambda_p$  below

the initial value and recovers only slightly over time (Table 4).

The tetragonal distortion of martensite correlates with its lattice parameter  $\alpha_{\text{bcc}}$  [35], which can be measured using XRD and the LPA. The results (Table 4) show a strong decrease of  $\alpha_{\text{bcc}}$  from the as-hardened to the annealed state after 1 s. After the first interval, the decrease in  $\alpha_{\text{bcc}}$  is much less pronounced, indicating that most of the relaxation is finished after 1 s. So the relaxation of martensite does not lead to a measurable increase of conductivity after 1 s.

In the second interval, starting after about 2 s, the volume fraction of cementite does not increase any further and the carbon content of the matrix has reached a value close to the equilibrium. Changes of the thermal and electrical conductivity are now dependent on changes in the content of substitutional elements in the matrix and Ostwald-ripening of the carbides.

Cr, Mn, and Si are the major substitutional impurities in the matrix. Both have a much lower diffusion rate in bcc matrix than carbon, and so it takes a much longer time to reach a matrix content close to equilibrium. In detail, Cr reaches the equilibrium content in the matrix after about 400,000 s and Mn and after 500,000 s. Ni and Si do not seem to reach the equilibrium until the end of the simulation, but the changes are very small at the end. Between 720 and 72,000 s, the mean levels of Cr and Mn in the bcc matrix are reduced from 0.19 to 0.07 at.% and 0.66 to 0.47 at.%, respectively. In contrast, the further reduction by tempering for 720,000 s is 0.02 at.% for Cr and 0.08 at.% for Mn only. Because of that, only a small increase of the thermal conductivity can be observed between 7200 and 720,000 s (see Fig. 4).

This increase can be related to the contents of Cr and Mn in the bcc matrix, because they both have a high impact on the conductivity [11]. After 720 s, the content of both has already decreased significantly. Since both are substitutional elements, they retard the electronic as well as the phononic heat transport, resulting in a nearly equal increase of  $\lambda_e$  and  $\lambda_p$ .

According to Gavriljuk et al., they decrease the state density at the Fermi level, thus reducing the number of conducting *s*-electrons [36, 37]. Additionally, the strain field induced by their different atomic size acts as a scattering center for phonons and electrons, which further reduces thermal and electrical conductivity [38].

Some effects take place in both intervals. This includes the reduction of lattice defects through recovery and recrystallization. The reduction of lattice defects is a comparatively fast process, taking place in the first minutes of the annealing. It incorporates several related processes, like the reduction of vacancies and dislocations and grain growth. All these processes cause a reduction of lattice defects, which results in a reduced number of scattering centers and leads to a higher phononic and electronic energy transport [39, 40]. Since their effect on the phononic transport is higher than on the electrical transport, their influence is merely visible in the short-term measurements of electrical conductivity.

Ostwald ripening also has an impact on the resulting electrical and thermal conductivity. After 720,000 s of annealing, the carbide size is about 2  $\mu\text{m}$ , so, as mentioned before, their direct contribution to conductivity is comparatively small [41]. Thus, since their volume fraction is constant after 2 s and their size grows constantly afterwards, the total number of carbides decreases (see Fig. 3b). This directly increases the mean free distance in the matrix, indirectly measured by the average particle distance shown in Fig. 3c. A longer mean free distance results in a lower number of scattering centers and therefore leads to a higher mobility of phonons, resulting in a higher phononic thermal conductivity after 72,000 s.

## Summary and conclusions

In this work, diffusion simulations of the cementite precipitation in the steel C45E were correlated with experimental data gained from quantitative image analysis and measurements of thermal and electrical conductivity after isothermal aging at 700 °C with dwell times from 1 to 720,000 s (200 h).

The experimental values agree well with the simulated data. By correlating both sources, it could be shown that the precipitation of cementite is finished within the first second regarding its volume fraction.

After that, the carbon content in the bcc matrix is constant and close to equilibrium. The diffusion simulations indicate two intervals of precipitation with different dominating effects with a different impact on the thermal and electrical conductivity: carbon-dominated and substitute-dominated. During the first two seconds of aging, the C-activity differs between matrix and cementite, resulting in LENP precipitation kinetics. This interval is dominated by the diffusion of carbon, the matrix contents of Cr, Mn, Si, and Ni do not change significantly. Additionally, martensite relaxation plays a role in this interval. In this stage, the thermal and electrical resistance of the cementite precipitates is overcompensated by the reduction of matrix resistance due to carbon depletion.

After 2 s, the equilibrium volume fraction of cementite is reached in the simulation. Quantitative image analysis confirms a constant volume fraction of about 6.6 vol.% between 720 and 720,000 s. In the same interval, the carbide size increases from 0.73 to 1.62  $\mu\text{m}$  due to Ostwald ripening, which is not considered by the diffusion simulation. In this second stage, the cementite volume fraction is constant, but its chemical composition is shifting towards equilibrium. Therefore, Cr, Mn and, to a much lower degree, Si and Ni diffuse into the carbide. The thermal and electrical conductivity increases slowly due to Ostwald ripening, defect healing and, most importantly, substitute depletion of the matrix. Ostwald ripening results in a longer mean free path (fewer precipitates) and a lower resistance of the precipitates due to a higher lattice/interface ratio. Matrix depletion from Cr and Mn results in less substitutional scattering centers and more free electrons due to a higher state density at the Fermi level.

The electrical and thermal conductivity is almost constant after 72,000 s (20 h) of isothermal tempering at 700 °C. Simulations show that the matrix content of Cr has nearly reached equilibrium at this time, while the Mn-content is decreasing slowly. Since the impact of Mn on the conductivity of the bcc matrix is much lower than that of Cr, the change in conductivity is much less pronounced.

It could be shown that both the depletion of carbon during the first stage as well as the substitute depletion in the second stage have a comparable quantitative influence on the thermal conductivity, but on very different time scales. The first stage takes only about 2 s, the second stage up to 200 h of

dwelling at a temperature as high as 700 °C. This has to be considered when designing heat-treatable steels for applications which require a specific thermal or electrical conductivity, especially since annealing temperatures are much lower in most cases.

## Acknowledgements

The authors acknowledge funding by the Deutsche Forschungsgemeinschaft (DFG) through the Project TH 531/13-2. *Influence of the solution condition and microstructure on the thermal and electrical conductivity of tool steels.*

**Open Access** This article is distributed under the terms of the Creative Commons Attribution 4.0 International License (<http://creativecommons.org/licenses/by/4.0/>), which permits unrestricted use, distribution, and reproduction in any medium, provided you give appropriate credit to the original author(s) and the source, provide a link to the Creative Commons license, and indicate if changes were made.

## References

- [1] Hamasaid A, Valls I, Heid R, Eibisch H (2012) A comparative experimental study on the use of two hot work tool steels for high pressure die casting of aluminum alloys: high thermal conductivity HTCS<sup>®</sup> and conventional 1.2343 (AISI H11). In: Leitner H, Kranz R, Tremmel A (eds) TOOL 2012: proceedings of the 9th international tooling conference: developing the world of tooling, 2012. Verlag Gutenberghaus, Knittelfeld
- [2] Wilzer J, Windmann M, Weber S, Hill H, van Bennekom A, Theisen W (2013) Thermal conductivity of advanced TiC reinforced metal matrix composites for polymer processing applications. *J Compos Mater*
- [3] Karbasian H, Tekkaya AE (2010) A review on hot stamping. *J Mater Process Technol* 210(15):2103–2118. doi:10.1016/j.jmatprotec.2010.07.019
- [4] Valls I, Casas B, Rodriguez N, Paar U (2010) Benefits from using high thermal conductivity tool steels in the hot forming of steels. *La Metall Ital* (11–12). <http://www.fracturae.com/index.php/aim/article/view/371>
- [5] Valls I, Casas B, Rodriguez N (2009) Importance of tool material thermal conductivity in the die longevity and product quality in HPDC. In: Beiss P, Broeckmann C, Franke S, Keysselsitz B (eds) Proceedings of the 8th international tooling conference, Aachen, 2009, vol 1. Verlag Mainz, Wissenschaftsverlag, pp 127–140
- [6] Wilzer J, Weber S, Escher C, Theisen W (2014) Werkstofftechnische Anforderungen an Press-härtewerkzeuge am Beispiel der Werkzeugstähle X38CrMoV5-3, 30MoW33-7 und 60MoCrW28-8-4. *HTM J Heat Treat Mater* 69(6):325–332
- [7] Wilzer JJ (2014) Wärmeleitfähigkeit martensitisch härtbarer Stähle: physikalische Zusammenhänge, Einflussfaktoren und technischer Nutzen. Dissertation, Ruhr-Universität Bochum, Bochum
- [8] Richter F, Kohlhaas R (1965) Wärmeleitfähigkeit des reinen Eisens zwischen –180 und 1000 °C unter besonderer Berücksichtigung von Phasenumwandlungen. *Archiv für das Eisenhüttenwesen* 36(11):827–833
- [9] Fulkerson W (1966) Comparison of the thermal conductivity, electrical resistivity, and Seebeck coefficient of a high-purity Iron and an Armco Iron to 1000 °C. *J Appl Phys* 37(7):2639–2653
- [10] Tritt TM (ed) (2010) Thermal conductivity: theory, properties, and applications. *Physics of solids and liquids*. Springer, New York
- [11] Terada Y, Ohkubo K, Mohri T, Suzuki T (2002) Effects of alloying additions on thermal conductivity of ferritic iron. *ISIJ Int* 42(3):322–324
- [12] Wilzer J, Küpferle J, Weber S, Theisen W (2015) Influence of alloying elements, heat treatment, and temperature on the thermal conductivity of heat treatable steels. *Steel Res Int* 86(11):1234–1241
- [13] Oppenkowski A, Weber S, Theisen W (2010) Evaluation of factors influencing deep cryogenic treatment that affect the properties of tool steels. *J Mater Process Technol* 210(14):1949–1955
- [14] Wilzer J, Lüdtke F, Weber S, Theisen W (2013) The influence of heat treatment and resulting microstructures on the thermophysical properties of martensitic steels. *J Mater Sci* 48(24):8483–8492. doi:10.1007/s10853-013-7665-2
- [15] Wilzer J, Küpferle J, Weber S, Theisen W (2014) Temperature-dependent thermal conductivities of non-alloyed and high-alloyed heat-treatable steels in the temperature range between 20 and 500 °C. *J Mater Sci* 49(14):4833–4843. doi:10.1007/s10853-014-8183-6
- [16] Abe H, Suzuki T (1980) Thermoelectric power versus electrical conductivity plot for quench-ageing of low-carbon aluminium-killed steel. *Trans Iron Steel Inst Jpn* 20(10):690–695
- [17] Abe H, Suzuki T, Mimura T (1982) Thermoelectric power vs. electrical conductivity plot for strain-ageing of low-carbon aluminium-killed steel. *Trans Iron Steel Inst Jpn* 22(8):624–628

- [18] Hanawa K, Mimura T (1984) Kinetics of precipitation from quenched low carbon steel. *Metall Trans A* 15(6):1147–1153
- [19] Song W, Choi P-P, Inden G, Prah U, Raabe D, Bleck W (2014) On the spheroidized carbide dissolution and elemental partitioning in high carbon bearing steel 100Cr<sub>6</sub>. *Metall Mater Trans A* 45(2):595–606
- [20] Rasband WS (1997–2015) ImageJ. US National Institutes of Health, Bethesda
- [21] Rietveld HM (1969) A profile refinement method for nuclear and magnetic structures. *J Appl Crystallogr* 2(2):65–71
- [22] Lutterotti L, Scardi P (1990) Simultaneous structure and size strain refinement by the Rietveld method. *J Appl Crystallogr* 23(4):246–252
- [23] Lutterotti L, Gialanella S (1998) X-ray diffraction characterization of heavily deformed metallic specimens. *Acta Mater* 46(1):101–110
- [24] Popa NC, Balzar D (2012) Elastic strain and stress determination by Rietveld refinement: generalized treatment for textured polycrystals for all Laue classes. *Corrigenda. J Appl Crystallogr* 45(4):838–839
- [25] Balzar D, Popa NC (2005) Analyzing microstructure by Rietveld refinement. *Rigaku J* 22(22):16–25
- [26] Hust JG (1983) Thermal conductivity and thermal diffusivity. In: Reed RP, Clark AF (eds) *Materials at low temperatures*. American Society for Metals, Metals Park, pp 133–161
- [27] Schneider A, Inden G (2005) Simulation of the kinetics of precipitation reactions in ferritic steels. *Acta Mater* 53(2):519–531
- [28] Inden G (2008) Kinetics of phase transformations in multi-component systems. In: Ghetta V, Gorse D, Mazière D, Pontikis V (eds) *Materials issues for generation IV systems*. NATO science for peace and security series. Springer, Heidelberg, pp 113–140
- [29] Roncery LM, Weber S, Theisen W (2011) Nucleation and precipitation kinetics of M<sub>23</sub>C<sub>6</sub> and M<sub>2</sub>N in an Fe–Mn–Cr–C–N austenitic matrix and their relationship with the sensitization phenomenon. *Acta Mater* 59(16):6275–6286
- [30] Shanina BD, Gavriljuk VG (2004) Effect of carbon and nitrogen on electronic structure of steel. *Steel Grips* 2:45–52
- [31] Gavriljuk VG, Shivanyuk VN, Shanina BD (2005) Change in the electron structure caused by C, N and H atoms in iron and its effect on their interaction with dislocations. *Acta Mater* 53(19):5017–5024
- [32] Hasselman DPH, Johnson LF (1987) Effective thermal conductivity of composites with interfacial thermal barrier resistance. *J Compos Mater* 21(6):508–515
- [33] Williams R, Graves R, Weaver F (1987) Effect of point defects on the phonon thermal conductivity of BCC iron. *J Appl Phys* 62(7):2778–2783
- [34] Granato A (1958) Thermal properties of mobile defects. *Phys Rev* 111(3):740–746
- [35] Saha DC, Biro E, Gerlich AP, Zhou Y (2016) Effects of tempering mode on the structural changes of martensite. *Mater Sci Eng A* 673:467–475
- [36] Shanina BD, Gavriljuk VG, Konchits AA, Kolesnik SP (1998) The influence of substitutional atoms upon the electron structure of the iron-based transition metal alloys. *J Phys Condens Matter* 10(8):1825–1838
- [37] Gavriljuk VG, Shanina BD, Berns H (2000) On the correlation between electron structure and short range atomic order in iron-based alloys. *Acta Mater* 48:3879–3893
- [38] Mott NF (1936) The electrical conductivity of transition metals. *Proc R Soc A* 153(880):699–717
- [39] Kraftmakher Y (1998) Equilibrium vacancies and thermo-physical properties of metals. *Phys Rep* 299(2–3):79–188
- [40] Madarasz F, Klemens P (1981) Phonon scattering by dislocations in metallic alloys. *Phys Rev B* 23(6)
- [41] Bhatt H, Donaldson KY, Hasselman DPH (1990) Role of the interfacial thermal barrier in the effective thermal diffusivity/conductivity of SiC-fiber-reinforced reaction-bonded silicon nitride. *J Am Ceram Soc* 73(2):312–316